

# Time evolution of high-energy emissions of low-mass stars:★,★★

## I. Age determination using stellar chronology with white dwarfs in wide binaries

A. Garcés,<sup>1</sup> S. Catalán,<sup>2</sup> I. Ribas<sup>1</sup>

<sup>1</sup> Institut de Ciències de l'Espai (IEEC-CSIC), Facultat de Ciències, Campus UAB, 08193 Bellaterra, Spain

<sup>2</sup> Centre for Astrophysics Research, University of Hertfordshire, College Lane, Hatfield, AL10 9AB, UK  
e-mail: garces@ice.csic.es, s.catalan@herts.ac.uk, iribas@ice.csic.es

Received 24 February 2011 / Accepted 30 March 2011

### ABSTRACT

**Context.** Stellar ages are extremely difficult to determine and often subject to large uncertainties, especially for field low-mass stars. We plan to carry out a calibration of the decrease in high-energy emissions of low-mass GKM stars with time, and therefore precise age determination is a key ingredient. The overall goal of our research is to study the time evolution of these high-energy emissions as an essential input to studying exoplanetary atmospheres.

**Aims.** We propose to determine stellar ages with a methodology based on wide binaries. We are interested in systems composed of a low-mass star and a white dwarf (WD), where the latter serves as a stellar chronometer for the system. We aim at obtaining reliable ages for a sample of late-type stars older than 1 Gyr.

**Methods.** We selected a sample of wide binaries composed by a DA type WD and a GKM companion. High signal-to-noise, low-resolution spectroscopic observations were obtained for most of the WD members of the sample. Atmospheric parameters were determined by fitting the spectroscopic data to appropriate WD models. The total ages of the systems were derived by using cooling sequences, an initial-final mass relationship and evolutionary tracks, to account for the progenitor life.

**Results.** The spectroscopic observations have allowed us to determine ages for the binary systems using WDs as cosmochronometers. We obtained reliable ages for 27 stars between 1 and 5 Gyr, which is a range where age determination becomes difficult for field objects. Roughly half of these systems have cooling ages that contribute at least 30% the total age. We select those for further study since their age estimate should be less prone to systematic errors coming from the initial-final mass relationship.

**Conclusions.** We have determined robust ages for a sizeable sample of GKM stars that can be subsequently used to study the time evolution of their emissions associated to stellar magnetic activity.

**Key words.** stars:low-mass, stars: white dwarfs, stars: visual binaries, stars: activity, stars: evolution

### 1. Introduction

The age of a star is one of the most difficult stellar parameters to determine. Although several age-dating methods are becoming more precise, stellar chronology still holds many uncertainties, especially when the objects are in the field and moderately old. For ages above 0.7 Gyr, open clusters and moving groups are, in general, not very useful as age calibrators, since they are typically at large distances, making their individual component stars difficult to study in detail, particularly their activity characteristics. This is clearly illustrated in recently proposed calibrations (Mamajek & Hillenbrand 2008) that, while providing good performance for young ages (15–20% uncertainty), do not yield accurate results beyond 0.5 Gyr because of the lack of calibrators and the increasing unreliability of rotation period estimates (differential rotation effects or a weak signal from low-amplitude

modulations). Furthermore, the calibrations are not applicable to stars later than K2.

The determination of the ages of low-mass stars has many applications in astrophysics (Mamajek & Hillenbrand 2008; Soderblom 2010), including the study of galactic populations or any use of intermediate-age G-, K-, and M- type stars as tracers of evolution, such as calibrating of the decrease in high-energy emissions. Our interest lies in this use of age calibrations for low-mass stars, because of the importance of stellar emissions, and their time variability, to the understanding of exoplanet atmospheres. The host star to a planet is, by far, its main source of energy, and many studies (e.g. Lammer et al. 2003; Penz et al. 2008) have demonstrated that stellar high-energy emissions have a strong impact on planetary atmospheres. Thus, characterizing such emissions is central to proper modelling of exoplanet properties. High-energy emissions are related to the magnetic activity of the star, and this activity decays throughout the stellar lifetime in an as yet poorly understood manner, making it difficult to calculate the accumulated effects of the UV and X-ray emission on the planetary environments. The decay in activity with stellar age is intimately linked to the rotational evolution of the stars (e.g. Skumanich 1972; Ayres 1997). Although the time evolution of high-energy emissions of solar-type stars is already well constrained from *The Sun in Time* project (Ribas et al. 2005), that of late GKM stars still needs much improvement. Our objective is

\* Based on observations collected at the Centro Astronómico Hispano Alemán (CAHA) at Calar Alto, operated jointly by the Max-Planck Institut für Astronomie and the Instituto de Astrofísica de Andalucía (CSIC)

\*\* Based on observations made with the WHT (William Herschel Telescope) operated on the island of La Palma by the Isaac Newton Group in the Spanish Observatorio del Roque de los Muchachos of the Instituto de Astrofísica de Canarias.

to extend *The Sun in Time* project to cooler stars. This is justified by the many differences in the high-energy emissions between, e.g., G-type and M-type stars and by the interest of the latter as hosts to exoplanets.

In this work we discuss the first part of our larger plan to determine age-activity relationships for low-mass stars in general. The paper is organised as follows. In §2 we present the results for stars with stellar ages below 0.7 Gyr. The methodology of the age determination for WDs is explained in §3. In §4 we collect our sample and describe its selection criteria. In §5 we present the observations and the data reduction. Section 6 is devoted to the analysis, atmospheric parameter determination, and the subsequent age determination method. This is followed by §7 where we discuss the low-mass companions in the context of defining age sequences, and finally in §8 we elaborate on our conclusions.

## 2. Preliminary work

We started by collecting data on the evolution of X-ray emissions for the younger stars (<1 Gyr). Their ages were determined from cluster and moving group membership (Montes et al. 2001), and the  $\log L_X$  values were obtained from a thorough list provided by Pizzolato et al. (2003). We complemented the measurements with X-ray data estimated directly from ROSAT measurements for some field stars with age estimates from different methods.

The young main sequence phase was studied by means of stars belonging to the IC2602, IC2391, Pleiades,  $\alpha$  Persei, Hyades clusters, and the Ursa Majoris moving group. The early G-type star sample, as we explained in section 1, was already available from *The Sun in Time* project. These stars have well-known rotation periods, temperatures, and metallicities. In general, we only consider stars in narrow spectral type bins (or effective temperature) to avoid contamination from the intrinsic variation in magnetic activity with stellar mass. The age range <0.07 Gyr is covered by stars in the IC2602, IC2391, and  $\alpha$  Persei clusters. We should point out that these clusters are younger than 0.07 Gyr, (0.03, 0.03, and 0.05 Gyr, respectively), but since saturation is present until 0.07 Gyr or longer in the case of K and M stars (Stepień et al. 2001; Jeffries et al. 2010), considering data with different ages does not affect the value of  $\log L_X$ .

For ages above 1 Gyr cluster or moving group membership is not a useful age determination method. Other age indicators, such as the use of rotation period, age-activity relations, asteroseismology, or theoretical isochrones, are more useful in this age domain. Some of them have been used to obtain the ages of a few GKM stars older than ~1 Gyr. Only a handful of field stars have reliable ages in this domain. These stars are  $\alpha$  Cen B and Proxima Cen, with ages determined from the isochrone and asteroseismologic age of their close companion  $\alpha$  Cen A (Porto de Mello et al. 2008). HR7703 shows space motions that are typical of a thick disk star, so we can very roughly assume an age of 10 Gyr. The X-ray luminosities of these stars were determined from the ROSAT database following the calibration in Schmitt et al. (1995). For stars older than ~6 Gyr long-term changes in high-energy emissions are, in general, difficult to distinguish from short-term stellar activity variations.

We have put together all the compiled data, and the evolution of  $\log L_X$  with age for three spectral type intervals (G0-5, K0-5, and M0-5) is illustrated in Fig. 1. In the case of G type stars, the plotted values are quite reliable as they come from a thorough analysis of the *The Sun in Time* sample. For K- and M-type stars, however, the plotted values are very crude results corresponding to the few stars described above that just have rough age estimates. It is likely that the uncertainty of each point is at

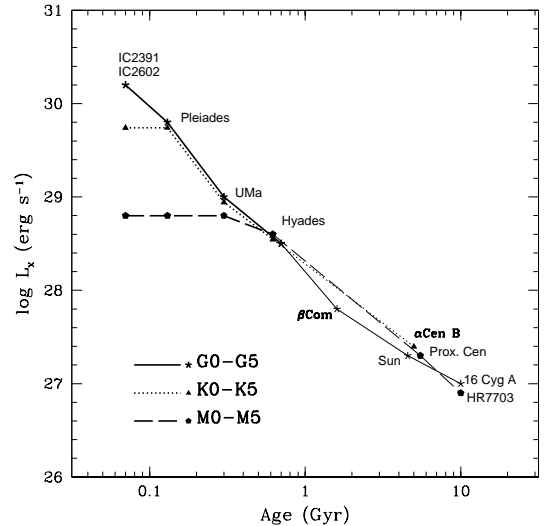


**Fig. 1.** X-ray luminosity versus age for solar-like stars and for field and cluster K- and M-type stars. Only a few K and M stars are available beyond 0.7 Gyr.

least of a few tenths of a dex. The figure shows, as expected, that M-type stars stay at saturated activity levels for a longer period of time than G-type stars. According to these results, solar-like G0-5 stars are at saturated emission levels until ages of ~100 Myr, and their X-ray luminosity decreases rapidly. K-type stars have saturated emission levels for a little longer (~200 Myr) and then also decrease rapidly. Finally, M0-M5 stars seem to have saturated emission levels up to 0.5 Gyr or more and then decrease in an analogous way to G- and K-type stars.

The interval corresponding to ages younger than ~0.7 Gyr is covered well by the used cluster and moving group stars (IC2602, IC2391, Pleiades,  $\alpha$  Persei, Hyades clusters, and the Ursa Majoris moving group), but it is obvious from our preliminary analysis that a more complete sample of older stars is needed to define reliable age-activity relationships. Furthermore, it is interesting to note that an age of 0.7 Gyr is a key point for our Sun, since it represents the time at which life is supposed to have appeared on the Earth's surface. Thus, data for older stars of different types will be very important for modelling planetary atmospheres in a regime that can be relevant to potential life on their surface, as happened to our Earth.

## 3. Methodology

We have developed an age determination method based on the use of wide binaries where one of the components, a WD, is used as a chronometer. The members of a wide binary are assumed to have been born simultaneously and with the same chemical composition. Since they are well separated (100-1000 AU), we can assume that no interaction has occurred between them in the past and they have evolved as single stars (Oswalt et al. 1988). We are interested in wide binaries composed by a WD and a star with GKM spectral type. The evolution of a WD can be described as a cooling process, which is relatively well understood at present (Salaris et al. 2000). The total age of the WD can be expressed as the sum of its cooling time plus the pre-WD lifetime of its progenitor. Thus, ages can be obtained from an initial-final mass relationship and stellar tracks to account for the pre-WD lifetime. This procedure is analogous to that described by Catalán et al.

(2008b). It is sound to assume that the age of the WD is the same as the that of the low-mass companion, since both members of a wide binary were born simultaneously.

We selected a sample of 30 wide binaries containing a WD and a GKM star (see Table 1). In the sample we favour WD components classified as a DA, i.e., with the unique presence of Balmer lines in their spectra. As we demonstrate in section 6, the fits to the spectral features of these WDs yield realistic values for the atmospheric parameters (effective temperature,  $T_{\text{eff}}$  and surface gravity,  $\log g$ ). We have collected a large amount of observational data (photometry and spectroscopy) on the WD components to implement the proposed approach. We aim at determining total system ages (i.e., cooling ages plus progenitor lifetime) with precisions of 10–20%. This is sufficient in our context since magnetic activity is an intrinsically variable phenomenon and any relationship will have some inherent dispersion no matter how accurate the ages and coronal/chromospheric fluxes.

#### 4. Sample selection

The sample of wide binaries was compiled from the available literature. For this we considered the recent revision of the New Luyten Two Tenths (NLTT) Catalogue (Luyten 1979-1980) by Chanamé & Gould (2004), an NLTT catalogue with Hipparcos stars from Gould & Chanamé (2004) and later completed with some pairs from a selection of WD+M systems made by Silvestri et al. (2005).

Our first selection was done only considering the catalogues of Chanamé & Gould (2004) and Gould & Chanamé (2004) and following a careful evaluation procedure. First, the WD component had to be classified as a DA (i.e., with the sole presence of Balmer lines), so that the fitting procedure can be sufficiently accurate to derive atmospheric parameters. Secondly, the other component of the pair should be a star of spectral type G, K, or M. For the WD type classification we have used the McCook & Sion (1999, 2006) catalogues, and the spectral classification of the low mass stars was made by calculating their  $V$ - $J$  index and taking the spectral classification into account for main sequence stars in Johnson et al. (1966). Information about the two proper motion components of both members of the wide binary is available in Chanamé & Gould (2004) and Gould & Chanamé (2004) catalogues for most of the members of the sample. We have completed and checked this information with data from USNO catalogue and calculated the total proper motion of each star. We only consider in our sample the wide binaries that satisfy the NLTT proper motion threshold,  $\mu \geq 180$  mas yr<sup>-1</sup> and that they show the same direction in their proper motions.

The resulting sample was completed considering some wide binaries from the catalogue of Silvestri et al. (2005). They studied the relationship between age and chromospheric activity for 189 binary systems composed of a WD and an M-type star. For this purpose, the authors determined the system's age using WDs as stellar clocks but assuming a rough value for their mass, the typical  $0.6M_{\odot}$  (Silvestri et al. 2001). Conversely, the ages estimated are potentially unreliable since the mass of each WD is an important parameter for estimating their progenitor lifetime. With the aim of improving age estimates, we performed a revision of the sample of Silvestri et al. (2005) and completed our sample by considering the pairs containing a DA WD and a GKM star in their catalogue. The targets from Silvestri et al. (2005) were also screened following the proper motion criteria explained in the previous paragraph.

**Table 1.** The wide binary sample. Spectral types are estimated from the  $V$ - $J$  index, except NLTT55287, for which  $B$ - $V$  was used.

White dwarf	$V$	Companion	$V$	$V$ - $J$	SpT.
NLTT1762	16.59	NLTT1759	10.28	1.46	K1
NLTT10976	17.20	NLTT10977	13.66	3.52	M2
NLTT13110	17.23	NLTT13109	12.63	3.21	M2
NLTT19311	16.58	NLTT19314	13.18	3.32	M2
NLTT21891	14.79	NLTT21892	15.41	4.22	M5
NLTT26379	12.92	NLTT26385	12.55	3.75	M4
NLTT28470	13.60	NLTT28469	14.09	4.13	M5
NLTT28712	15.55	NLTT28711	15.55	4.19	M5
NLTT28772	16.67	NLTT28771	16.72	4.18	M5
NLTT29967	17.26	NLTT29948	9.96	1.89	K4
NLTT31644	15.50	NLTT31647	16.89	5.06	M6
NLTT31890	15.86	NLTT31888	13.48	2.95	M0
NLTT39605	16.24	NLTT39608	15.74	3.85	M4
NLTT44348	17.50	NLTT44344	11.46	2.34	K7
NLTT56546	15.90	NLTT56548	16.60	3.99	M4
NLTT58107	16.13	NLTT58108	16.13	5.80:	M8
G86-B1B	16.10	G86-B1A	14.26	3.67	M4
LP347-4	12.92	LP347-5	11.70	3.82	M3
LP856-53	15.00	LP856-54	12.18	2.97	M0
LP888-64	13.56	LP888-63	13.80	4.23	M5
WOLF672A	14.34	WOLF672B	14.05	4.19	M4
NLTT4615	17.48	NLTT4616	12.44	3.13	M1
NLTT7890	17.39	NLTT7887	9.84	1.90	K3
NLTT15796	17.21	NLTT15797	15.46	4.31	M5
G107-70	14.62	G107-69	13.52	4.38	M6
NLTT1374	16.22	NLTT1370	12.90	2.19	K6
NLTT7051	16.18	NLTT7055	13.06	2.97	M0
NLTT13599	15.94	NLTT13601	8.42	2.47	K7
NLTT55288	16.50	NLTT55287	8.03	1.21	G7
L577-71	12.80	L577-72	13.56	4.08	M4

Our final sample is composed of 30 wide binaries. The sample with all relevant information, including the  $V$ - $J$  indices of the companions and their inferred spectral types, is provided in Table 1. For NLTT55287  $J$  photometry was not available and the spectral type was determined from the  $B$ - $V$  index. In Table 1 we provide an approximate value for  $V$ - $J$  corresponding to an M8 star. Although photometric information about the two members of the binary was available in the catalogues, we checked all  $V$  magnitudes in the SIMBAD database. We found some differences or confusions between the magnitudes of the two members in some cases. For these targets we made a thorough analysis to make sure that each member was correctly identified. Figure 2 shows a histogram with the spectral type distribution of the low-mass stars. As can be seen, most of the sample is composed by M-type stars plus a few K-type stars and one G-type star. As we discuss in section 6, the WD sample mainly contains DA-type WDs, but also a few DC-type WDs.

#### 5. Observations and data reduction

We performed optical long-slit low-resolution spectroscopic observations for our analysis, with the goal of obtaining measurements with high signal-to-noise ratio ( $\sim 75$ – $100$ ). We were able to obtain spectroscopic data for 25 WDs in our sample during different observing campaigns between February of 2009 and February of 2010. The observing runs were carried out at Observatorio del Roque de los Muchachos (ORM) and the German-Spanish Astronomical Center at Calar Alto (CAHA). The 3.5m telescope was used during three nights in February of 2009 at CAHA, and the William Herschel Telescope (WHT) dur-

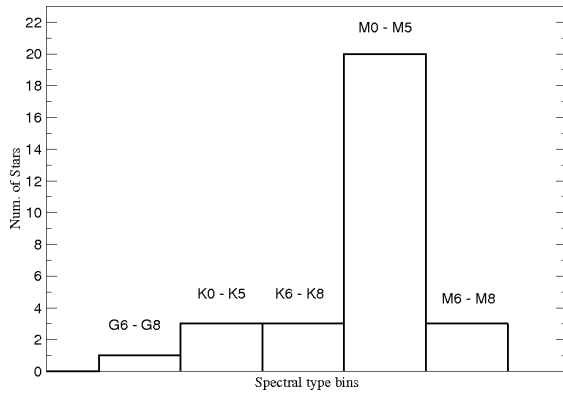


**Fig. 2.** Histogram of the spectral type distribution of the low-mass stars in our sample, which are mostly of spectral type M.

**Table 2.** Information about the setup used for each observatory.

Observ.	Telesc.	Spectrogr.	R	Arm	Grism	Spectral coverage(Å)
CAHA	3.5m	TWIN	1250	Red	T04	5500–7500
				Blue	T08	3500–6500
ORM	WHT	ISIS	2600	Red	R316R	4570–8430
				Blue	R300B	2730–6270

ing 4.5 nights in February and September of 2009 and February of 2010 at ORM. Table 2 provides more details about the observation setups used. We managed to observe 25 out of 30 initial targets, with the remaining five not visible at the time the observing runs were allocated.

The spectroscopic observations covered the main H Balmer lines, from  $H\alpha$  to  $H\epsilon$  or  $H9$ , whenever possible. The two spectrographs used included two separate spectroscopic channels (blue and red arms) behind the common entrance slit aperture. We chose a proper dichroic position in order to observe the  $H\alpha$  line in the red arm and all the other visible Balmer lines in the blue arm, covering at least a spectral range of  $\sim 3500\text{--}7500\text{ \AA}$ . A suitable grism selection was done to place  $H\alpha$  centred and unvignetted for the red arm and a maximum number of unvignetted Balmer lines for the blue arm. The slit width for each observation was chosen according to the seeing ( $\sim 1''\text{--}2''$ ). Spectra of high quality are essential to derive the atmospheric parameters with accuracy. We performed as many exposures as necessary to guarantee a high signal-to-noise ratio ( $\sim 75\text{--}100$ ) for the final spectrum of each object (after the corresponding reduction). The exposure times and signal-to-noise ratios for all the targets are shown in Table 3. For targets with individual observations with low signal-to-noise ratio, we co-added individual 1800 s exposures to minimise the effects of cosmic ray hits on the CCD.

The WD spectra were reduced using the standard procedures within the single-slit tasks of IRAF<sup>1</sup>. First, the images were bias-corrected and flatfield-normalised, and then, the spectra were extracted and wavelength-calibrated using arc lamp observations. Flux calibrations were not performed since they are not necessary for our subsequent analysis, and most of the nights were not photometric. We applied the heliocentric correction to

<sup>1</sup> IRAF is distributed by the National Optical Astronomy observatory, which are operated by the Association of Universities for Research in Astronomy, Inc., under cooperative agreement with the National Science Foundation <http://iraf.noao.edu>

**Table 3.** Observation details for the targets in the sample.

Observed target	Exp. time (sec)	S/N	Num. of exposures
NLTT1762	9000	165	5
NLTT4615	1800	20	1
NLTT7890	3600	50	2
NLTT10976	7200	75	4
NLTT13110	3600	80	2
NLTT15796	7200	105	4
NLTT19311	12600	160	7
NLTT21891	5100	320	5
NLTT26379	1200	330	5
NLTT28470	1500	290	5
NLTT28712	6300	165	5
NLTT28772	13500	190	9
NLTT29967	12600	185	7
NLTT31644	7200	285	6
NLTT31890	7200	140	4
NLTT39605	7200	120	4
NLTT44348	7200	100	4
NLTT56546	3600	140	2
NLTT58107	3600	190	2
G86-B1B	11700	210	8
G107-70	3500	120	3
LP347-4	500	130	2
LP856-53	4500	210	5
LP888-64	400	120	2
WOLF672A	4200	350	6

each spectrum prior to coadding multiple observations obtained in different nights.

## 6. White dwarf analysis

After the corresponding reduction, we carried out a first inspection of the spectra. Although all the WDs we selected had previously been classified as DA, we found that four of them do not show the bluer Balmer lines in their spectra, so they are likely to be the DC type. For these four targets we checked the part of the spectrum observed with the red arm. The  $H\alpha$  line was not visible in any of them, and is faint in DC WDs, the resolution of the instrument and the low signal-to-noise ratio of the spectrum yields in the absence of such line for these four spectra. Table 1 lists the observed 21 DA type WDs in the first set of rows and remaining four observed DCs in the second set of rows.

Once the spectra of the DA targets were correctly selected, we proceeded to the continuum normalization procedure. The normalization has to be carried out carefully because the determination of atmospheric parameters is very sensitive to variations in the continuum. We carefully defined several clean continuum windows by considering the central part of each spectrum and avoiding any irregular feature or the wings of the spectral lines. We used Legendre polynomials of order 15 to 20 for the normalization procedure.

### 6.1. Atmospheric parameters

Before calculating the atmospheric parameters of the WDs ( $T_{\text{eff}}$  and  $\log g$ ), we determined the radial velocities of each star using the IRAF task `FXCOR`. Each spectrum was cross-correlated with a reference model from a grid computed by D. Koester. The resulting radial velocity values can be found in Table 4. The radial velocities determined were small in a number of cases (ranging from 10 to 90  $\text{km s}^{-1}$ ) when compared with the resolution

element of our observations. For some of the stars, however, the measured radial velocities were higher (ranging from 100 to 200 km s<sup>-1</sup>) thus becoming relevant to the subsequent analysis. In our procedure we took all the radial velocities for consistency into account.

We derived the atmospheric parameters of the WDs by performing a fit of the observed Balmer lines using the models of D. Koester (private communication), following a procedure based on  $\chi^2$  minimization. The Balmer lines in such WD models were calculated with the modified Stark broadening profiles of Tremblay & Bergeron (2009), kindly made available by the authors. The model grid used covers the range  $T_{\text{eff}}=5000\text{--}100000$  K, in steps of 1000 K at low temperatures ( $T_{\text{eff}} < 14000$  K), steps of 2000 K (from  $T_{\text{eff}} = 16000$  to 20000 K), steps of 5000 K (from  $T_{\text{eff}} = 20000$  to 40000 K), and steps of 10000 K for the higher temperatures ( $T_{\text{eff}} > 40000$  K). The range of  $\log g$  is between 5.0 and 9.0 steps of 0.5 dex. The WD models had been previously normalised to the continuum and convolved with a Gaussian instrumental profile with the proper FWHM in order to have the same resolution as the observed spectra. The fit of the line profiles to synthetic models was done using a subroutine based on the SIMPLEX  $\chi^2$  minimization method of Press et al. (1992). We observed that the fitting procedure applied to all the observed lines (in the red and blue arms) suffered from considerable systematic effects. After running a number of tests we decided to consider only the lines observed with the blue arm for the analysis to avoid systematic errors because the H $\alpha$  line in the red arm is less adequate for atmospheric parameter determination.

Both  $T_{\text{eff}}$  and  $\log g$  were obtained simultaneously. It is well known that the changes in the profiles of the Balmer lines induce a certain degree of degeneracy to the procedure. There are often two numerically valid solutions corresponding to minima of the  $\chi^2$  function around the maximum strength of the Balmer lines ( $T_{\text{eff}} \approx 12000$  K), i.e., a “cool” and a “hot” solution. In some cases these two minima are well separated and their individual determination is straightforward. But for some other objects, the parameters corresponding to the two scenarios are so close as to become harder to distinguish. We tried to obtain both solutions for the WDs by changing the initial  $T_{\text{eff}}$  for the analysis. We were able to distinguish between the “cool” and “hot” solutions by finding the minimum value of  $\chi^2$  for both cases and comparing the results with the photometric temperatures obtained as explained in section 6.2.

Given that our spectra have a very high signal-to-noise ratio, the main contributor to the uncertainty in the fitting process (besides the adequacy of the models themselves) is the normalization procedure. The normalization can potentially modify the broad profiles of the spectral lines and thus introduce systematic errors in the resulting parameters. We carried out a careful analysis to quantify such an error source. Using the IRAF CONTINUUM task, we obtained the blaze functions for each individual spectrum. To do so, we devised a procedure that is based on normalizing each individual spectrum with the blaze functions corresponding to all the remaining spectra taken with the same instrument. Each of the resulting spectra was then re-normalised (to correct for obvious trends) employing a 5-order Legendre function for the observations with higher signal-to-noise and order 3 for the ones with low signal-to-noise ratio. Finally, each of the resulting spectra for every target were fitted to models as explained above to determine the atmospheric parameters. The final uncertainties were estimated following the prescription of Bergeron et al. (1992), i.e., by deriving them from the independent fits of the individual exposures for any given star before combination, but in our case by considering all the normalised

**Table 4.** Atmospheric parameters determined from fits to the Balmer lines to the observed WDs of our sample and radial velocity values obtained for them.

WD Name	$T_{\text{eff}}$ (K)	$\log g$ (dex)	Radial velocity (km s <sup>-1</sup> )
NLTT1762	10360±200	8.19±0.15	185±30
NLTT13110	6630±220	7.99±0.19	210±15
NLTT19311	7600±90	7.88±0.16	30±15
NLTT21891	13520±580	7.92±0.07	110±40
NLTT26379	15150±590	7.91±0.08	110±40
NLTT28470	15290±570	7.99±0.08	20±5
NLTT28712	9910±250	8.04±0.16	125±30
NLTT28772	9720±190	8.09±0.11	85±20
NLTT31644	19180±500	7.89±0.15	160±40
NLTT31890	10790±290	8.17±0.07	5±5
NLTT39605	9280±230	8.12±0.11	5±5
NLTT56546	13660±540	7.97±0.10	50±10
NLTT58107	11130±380	8.05±0.09	50±10
G86-B1B	9100±220	8.12±0.11	160±20
LP347-4	12760±230	7.91±0.05	90±30
LP856-53	10200±260	8.26±0.15	165±30
LP888-64	9530±310	7.92±0.12	50±25
WOLF672A	13330±570	7.85±0.10	15±5
NLTT10976	7050±190	7.68±0.25	115±20
NLTT29967	6180±220	7.26±0.45	170±40
NLTT44348	6510±190	7.42±0.33	-40±10

**Notes.** The last three rows correspond to objects for which the fit is poor.

individual spectra. We are aware that this procedure may overestimate the error since some of the renormalised spectra were clearly not optimal. However, we prefer to make certain that all possible systematic errors in the fitting procedure are accounted for by taking a conservative approach and considering the uncertainties derived in this way. The results of the fits and the estimated uncertainties are shown in Table 4. Figures 3 and 4 show the fits to the Balmer line profiles for the DA WDs in our sample.

## 6.2. Photometric effective temperatures

Some stars in our sample were not visible in the epochs of our observing runs. For these stars, and for the ones with no Balmer lines in their spectrum, we used the available IR photometry to obtain their photometric  $T_{\text{eff}}$ . The  $V$  magnitudes were obtained from the catalogues used to build the sample and from the SIMBAD database,  $JHK$  photometry was collected from the 2MASS All Sky Catalog when available. For  $V$  magnitude we assumed an uncertainty of 0.02 mag as errors are seldom available.

The  $T_{\text{eff}}$  for each object was obtained by adapting the method of Masana et al. (2006) to WDs. This procedure consists in calculating synthetic photometry using the WD atmospheres of Holberg & Bergeron (2006). Subsequently, we developed a fitting algorithm to compare the observational and theoretical values and minimise the  $\chi^2$  using the Levenberg-Marquardt method, and  $\chi^2$  was defined from the differences between the observed and synthetic  $VJHK$  magnitudes. The uncertainties in the calculated photometric temperatures were derived from the covariance matrix. The  $VJHK$  magnitudes and photometric  $T_{\text{eff}}$  for the sample stars are provided in Table 5.

In the cases where both spectroscopic data and  $V$  and  $JHK$  2MASS photometry were available, the photometric  $T_{\text{eff}}$  was

**Table 5.** *VJHK* magnitudes and photometric  $T_{\text{eff}}$  derived for the stars in our sample.

WD	<i>V</i>	<i>J</i>	<i>H</i>	<i>K</i>	$T_{\text{eff}}$ (K)
NLTT10976	17.20±0.02	16.801±0.150	15.205±0.202	15.783±0.232	7220±340
NLTT19311	16.58±0.02	16.070±0.103	15.833±0.194	15.583±0.220	7760±320
NLTT21891	14.79±0.02	14.962±0.041	15.127±0.055	15.055±0.167	12700±670
NLTT26379	12.92±0.02	13.405±0.026	13.445±0.030	13.544±0.056	18880±1210
NLTT28470	13.60±0.02	14.013±0.036	13.984±0.059	14.026±0.082	15640±1150
NLTT28712	15.55±0.02	15.591±0.057	15.483±0.100	15.734±0.177	10700±380
NLTT29967	17.26±0.02	16.018±0.087	15.684±0.114	15.500±0.238	5620±160
NLTT31890	15.86±0.02	15.802±0.067	15.627±0.136	15.721±0.217	9980±320
NLTT39605	16.24±0.02	16.052±0.075	15.722±0.122	15.889±0.279	9100±290
NLTT56546	15.90±0.02	16.571±0.137	15.995±0.197	15.522±0.264	13640±1050
G86-B1B	16.10±0.02	16.038±0.078	15.565±0.114	14.562±0.109	8598±240
LP347-4	12.92±0.02	13.171±0.029	13.195±0.037	13.179±0.028	12640±500
LP856-53	15.00±0.02	14.907±0.110	14.797±0.249	14.754±0.227	9800±450
LP888-64	13.56±0.02	13.188±0.067	13.205±0.061	13.174±0.098	8940±190
WOLF672A	14.26±0.02	14.603±0.056	14.534±0.070	14.562±0.109	13600±960
NLTT4615	17.48±0.02	16.466±0.098	16.245±0.193	15.555±0.181	5950±190
NLTT7890	17.39±0.02	16.131±0.081	16.131±0.081	16.048±0.165	5600±160
NLTT15796	17.23±0.02	15.712±0.057	15.461±0.078	15.511±0.155	5025±60
G107-70	14.62±0.02	13.083±0.022	12.838±0.022	12.756±0.025	5200±60
NLTT1374	16.22±0.02	16.050±0.082	15.842±0.168	15.676±0.248	9290±320
NLTT7051	16.18±0.02	15.568±0.059	15.392±0.124	15.353±0.206	7630±220
NLTT13599	15.94±0.02	14.598±0.038	14.232±0.058	14.136±0.069	5400±80
NLTT55288	16.50±0.02	15.629±0.067	15.279±0.086	15.195±0.168	6510±170
L577-71	12.80±0.02	13.183±0.033	12.885±0.033	12.794±0.034	11310±300

**Notes.** The table is divided into three sections: the first one contains the observed DA WDs, the second one lists the DC WDs, and the third one includes the WDs that have no spectroscopic observations.

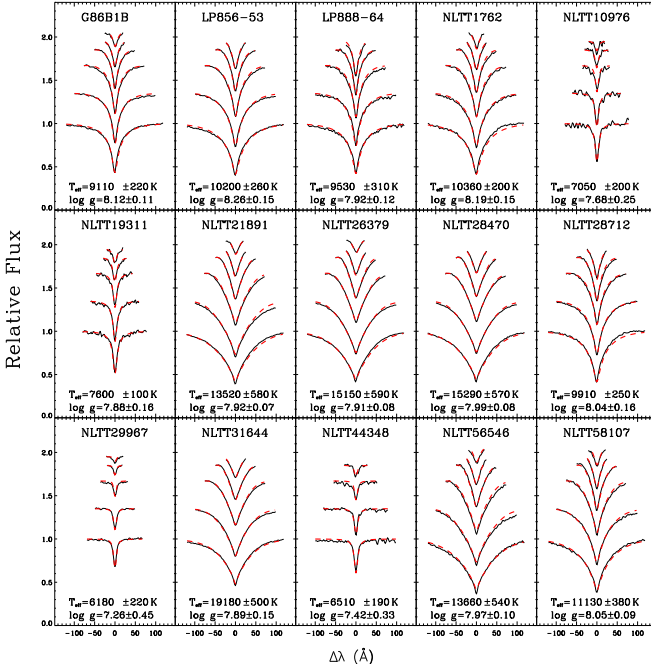


**Fig. 3.** Fits to the individual Balmer lines for the WDs observed at the WHT of ORM. The line profiles correspond to  $H\beta$  (bottom) up to  $H\epsilon$ , H8, or H9 (top) depending on the object. We have applied vertical shifts for clarity. The solid lines are the observed spectra and the dashed lines the model that best fits the profile.

used to evaluate the reliability of the resulting  $T_{\text{eff}}$  obtained by the line profile analysis. In most of the cases, both  $T_{\text{eff}}$  were in good agreement, as shown in Fig. 5. NLTT26379 is the object showing the largest deviation. For our subsequent analysis,

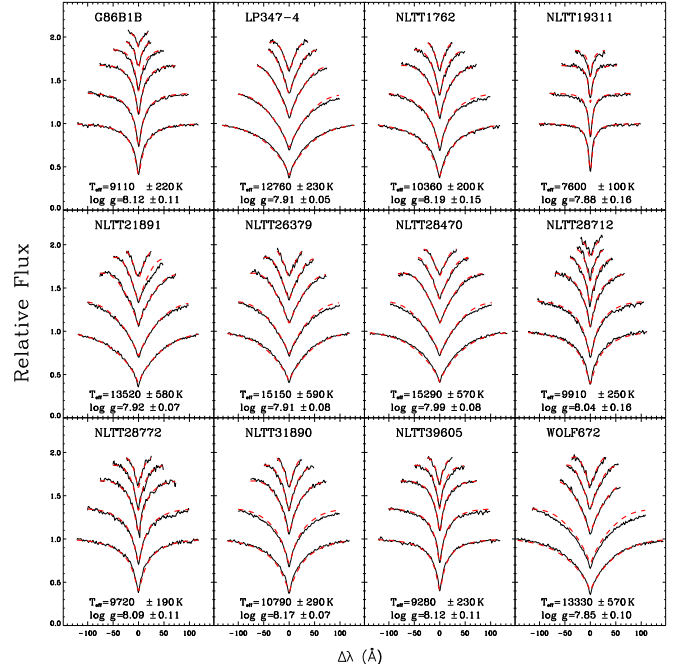


**Fig. 4.** Same as Fig. 3 for the WDs observed at the 3.5-m telescope at CAHA.

we consider the  $T_{\text{eff}}$  value obtained from spectroscopy, since it should be more reliable. It is worth noting that the spectroscopic analysis of WDs with  $T_{\text{eff}} < 12000\text{K}$  should be done with special care, since their atmospheres could be enriched in helium while retaining their DA spectral type (Bergeron et al. 1992). In this case, photometric  $T_{\text{eff}}$  provide the needed cross-check to ensure that the overall atmospheric parameters are consistent and accu-

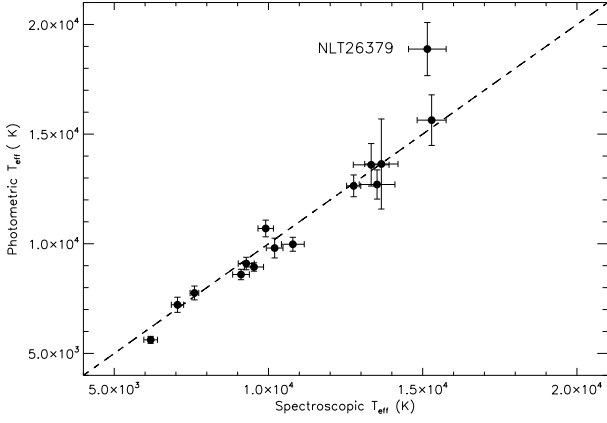


**Fig. 5.** Comparison of photometric and spectroscopic  $T_{\text{eff}}$  derived in this work for 15 WDs in our sample. The dashed line indicates 1:1 correspondence. The  $\chi^2$  of the difference between the measurements is 0.57.

rate. It is reassuring to confirm that our photometric and spectroscopic  $T_{\text{eff}}$  values are in good concordance for the cooler targets of our sample.

Together with  $T_{\text{eff}}$ , our procedure requires a value for  $\log g$ . Given the absence of any other possibility for the objects with photometric  $T_{\text{eff}}$ , we decided to adopt a “mean”  $\log g$  estimated from the WDs in the sample with spectroscopic parameters. We employed all WDs with reliable  $\log g$  values (i.e., the first part of Table 4). We obtained  $\log g = 8.01 \pm 0.20$ , in which the error bar is not the standard deviation but the overall range.

### 6.3. Masses, cooling times and total ages

Once we derived the  $T_{\text{eff}}$  and  $\log g$  of each WD, its mass ( $M_{\text{WD}}$ ) and cooling time ( $t_{\text{cool}}$ ) can be obtained by using the appropriate cooling sequences. We have adopted the cooling tracks of Salaris et al. (2000), which consider a carbon-oxygen (C/O) core WD (with a higher abundance of O at the central core) with a thick hydrogen envelope on top of a helium buffer,  $q(\text{H}) = M_{\text{H}}/M = 10^{-4}$  and  $q(\text{He}) = M_{\text{He}}/M = 10^{-2}$ . These improved cooling sequences include an accurate treatment of the crystallization process of the C/O core, including phase separation upon crystallization, together with up-to-date input physics suitable for computing WD evolution. The resulting values for  $M_{\text{WD}}$  and  $t_{\text{cool}}$  are listed in Table 7.

Systematic errors related to uncertainties on the CO stratification and envelope composition may affect the cooling sequences (Salaris 2009). To check the sensitivity of our results to the adopted cooling tracks, we also used the sequences of Fontaine et al. (2001), which consider different core and envelope compositions. The composition of the cooling sequences employed can be found in Table 6. The derived masses do not change appreciably when adopting alternative cooling sequences, with differences less than  $\sim 0.02 M_{\odot}$  over the entire mass range. The average of the differences in  $t_{\text{cool}}$  were found to be around 9%. Thus, we adopted a systematic error of 9% in  $t_{\text{cool}}$  in our subsequent analysis of the cooling ages.

For three of our targets, included at the bottom of Table 4, our spectroscopic fitting procedure yielded low values of  $\log g$  ( $< 7.7$ ) with relatively poor fits. The photometric temperatures available for two of these targets (NLTT10976 and NLTT29967) show good agreement with the spectroscopic value, thus indi-

**Table 6.** Cooling sequences, and layer composition.

Sequences	Core	H envelope $q(\text{H})$	He buffer $q(\text{He})$
Salaris et al. (2000)	C/O	$10^{-4}$	$10^{-2}$
Fontaine et al. (2001)	pure C	$10^{-4}$	$10^{-2}$
	50/50 C/O	$10^{-4}$	$10^{-2}$
	50/50 C/O	$10^{-10}$	$10^{-2}$

cating the consistency of the analysis. Thus, although the  $\log g$  values that we obtained seem reliable, we could not infer reliable masses for them using the cooling sequences of Salaris et al. (2000) since they are out of the covered parameter range. The values for  $M_{\text{WD}}$  and  $t_{\text{cool}}$  obtained via extrapolation for these three targets can be found in Table 7. We obtained  $M_{\text{WD}} < 0.5 M_{\odot}$ , which yields progenitor masses lower than  $1 M_{\odot}$ .

From the derived  $M_{\text{WD}}$  and  $t_{\text{cool}}$  values, the mass of the progenitor ( $M_{\text{prog}}$ ) can be determined using an initial-final mass relationship (Catalán et al. 2008a). From the calculated  $M_{\text{prog}}$ , we used the stellar tracks of Domínguez et al. (1999) to derive the progenitor’s lifetime ( $t_{\text{prog}}$ ). The total age of the WDs, and consequently that of the low-mass companion, follows directly by adding  $t_{\text{prog}}$  and  $t_{\text{cool}}$ . The final age value is provided in Table 7. In this Table we compiled the final atmospheric parameters, the mass of the WD, the mass of the progenitor star, the cooling time of the WD, the main-sequence time of the progenitor star, the total age, the ratio between the cooling time and the total age, and the  $V-J$  colour of the low-mass companions. The first 18 WDs in the Table have atmospheric parameters determined from the Balmer line profile fitting. The three objects in the middle were analysed spectroscopically, but the derived  $\log g$  are outside of the valid parameter range of our procedure. The nine WDs at the end of the table have temperatures determined by  $VJHK$  photometry and the mean  $\log g$  value for our sample estimated from the spectroscopic determinations.

Some of the WDs in our sample have atmospheric parameters and, in some cases, masses, cooling times, and ages estimated from previous investigations, such as Bergeron et al. (2001), Silvestri et al. (2001), Gianninas et al. (2005), and Zhao et al. (2011). We can compare our results to the previous determination. Our  $T_{\text{eff}}$  and  $\log g$  values are compared to those in the literature and are shown in Fig. 6. In general the agreement between the  $T_{\text{eff}}$  determinations is good within the uncertainties, but there are some discrepant results for some of the targets, such as NLTT26379 and G86-B1B. In the case of G86-B1B, our analysis shows good accord between spectroscopic and photometric determinations and thus, given the available cross-check, we prefer the value we determined. In the case of NLTT26379, our photometric and spectroscopic  $T_{\text{eff}}$ s are discrepant at the  $2.7\text{-}\sigma$  level, and the result of Silvestri et al. (2001) (using photometry) lies squarely in between. Given the better a priori reliability of the line profile analysis for  $T_{\text{eff}}$  above 12000 K, we subsequently adopt the spectroscopic  $T_{\text{eff}}$  value. The comparison of the  $\log g$  values between our values and the literature yields no very discrepant results.

### 6.4. Photometric distances

We have collected available parallax measurements for the low-mass companions and completed the information with photometric distances. The photometric distances were determined using the evolutionary models for low-mass stars described in Baraffe et al. (1997) and using the ages determined for each

**Table 7.** Main results for the WDs in our sample.

WD	$T_{\text{eff}}$ (K)	$\log g$	$M_{\text{WD}}$ ( $M_{\odot}$ )	$t_{\text{cool}}$ (Gyr)	$M_{\text{prog}}$ ( $M_{\odot}$ )	$t_{\text{prog}}$ (Gyr)	Age (Gyr)	$t_{\text{cool}}/\text{Age}$ (%)	Comp V-J
<b>NLTT1762</b>	<b>10360±200</b>	<b>8.19±0.15</b>	<b>0.72±0.07</b>	<b>0.68±0.10</b>	<b>2.96±0.52</b>	<b>0.49<sup>+0.11</sup><sub>-0.10</sub></b>	<b>1.2<sup>+0.15</sup><sub>-0.14</sub></b>	<b>58</b>	<b>1.46</b>
<b>NLTT13110</b>	<b>6630±220</b>	<b>7.99±0.19</b>	<b>0.59±0.08</b>	<b>1.61±0.35</b>	<b>1.64±0.87</b>	<b>2.3<sup>+2.6</sup><sub>-1.1</sub></b>	<b>3.9<sup>+2.6</sup><sub>-1.1</sub></b>	<b>42</b>	<b>3.21</b>
NLTT19311	7600±100	7.88±0.16	0.52±0.07	0.94±0.13	0.96±0.73	12 <sup>+8</sup> <sub>-10</sub>	13 <sup>+8</sup> <sub>-10</sub>	7	3.32
NLTT21891	13520±580	7.92±0.07	0.57±0.03	0.23±0.03	1.45±0.32	3.4 <sup>+1.1</sup> <sub>-1.0</sub>	3.6 <sup>+1.1</sup> <sub>-1.0</sub>	6	4.22
NLTT26379	15150±590	7.91±0.08	0.56±0.03	0.16±0.02	1.41±0.36	3.8 <sup>+1.4</sup> <sub>-1.3</sub>	3.9 <sup>+1.4</sup> <sub>-1.3</sub>	4	3.75
NLTT28470	15290±570	7.99±0.08	0.61±0.03	0.18±0.02	1.86±0.38	1.49 <sup>+0.47</sup> <sub>-0.29</sub>	1.67 <sup>+0.47</sup> <sub>-0.29</sub>	11	4.13
<b>NLTT28712</b>	<b>9910±250</b>	<b>8.04±0.16</b>	<b>0.63±0.07</b>	<b>0.62±0.09</b>	<b>2.05±0.74</b>	<b>1.15<sup>+0.71</sup><sub>-0.34</sub></b>	<b>1.77<sup>+0.71</sup><sub>-0.35</sub></b>	<b>35</b>	<b>4.19</b>
<b>NLTT28772</b>	<b>9720±190</b>	<b>8.09±0.11</b>	<b>0.65±0.05</b>	<b>0.69±0.08</b>	<b>2.32±0.55</b>	<b>0.89<sup>+0.26</sup><sub>-0.19</sub></b>	<b>1.58<sup>+0.27</sup><sub>-0.20</sub></b>	<b>44</b>	<b>4.18</b>
NLTT31644	19180±500	7.89±0.15	0.57±0.06	0.07±0.01	1.44±0.61	3.5 <sup>+2.8</sup> <sub>-1.7</sub>	3.5 <sup>+2.8</sup> <sub>-1.7</sub>	2	5.06
<b>NLTT31890</b>	<b>10790±290</b>	<b>8.17±0.07</b>	<b>0.71±0.03</b>	<b>0.60±0.06</b>	<b>2.88±0.29</b>	<b>0.53<sup>+0.07</sup><sub>-0.06</sub></b>	<b>1.13<sup>+0.09</sup><sub>-0.09</sub></b>	<b>53</b>	<b>2.95</b>
<b>NLTT39605</b>	<b>9280±230</b>	<b>8.12±0.11</b>	<b>0.67±0.05</b>	<b>0.82±0.10</b>	<b>2.52±0.55</b>	<b>0.76<sup>+0.17</sup><sub>-0.18</sub></b>	<b>1.58<sup>+0.19</sup><sub>-0.20</sub></b>	<b>52</b>	<b>3.85</b>
NLTT56546	13660±540	7.97±0.10	0.59±0.04	0.24±0.03	1.72±0.45	1.93 <sup>+0.87</sup> <sub>-0.54</sub>	2.17 <sup>+0.87</sup> <sub>-0.54</sub>	11	3.99
<b>NLTT58107</b>	<b>11130±380</b>	<b>8.05±0.09</b>	<b>0.64±0.04</b>	<b>0.47±0.05</b>	<b>2.15±0.45</b>	<b>1.04<sup>+0.30</sup><sub>-0.18</sub></b>	<b>1.51<sup>+0.30</sup><sub>-0.19</sub></b>	<b>31</b>	<b>5.80:</b>
<b>G86-B1B</b>	<b>9110±220</b>	<b>8.12±0.11</b>	<b>0.67±0.05</b>	<b>0.86±0.10</b>	<b>2.51±0.56</b>	<b>0.77<sup>+0.18</sup><sub>-0.19</sub></b>	<b>1.64<sup>+0.21</sup><sub>-0.22</sub></b>	<b>53</b>	<b>3.67</b>
LP347-4	12760±230	7.91±0.05	0.56±0.02	0.27±0.03	1.36±0.26	4.3 <sup>+1.0</sup> <sub>-1.1</sub>	4.5 <sup>+1.0</sup> <sub>-1.1</sub>	6	3.82
<b>LP856-53</b>	<b>10200±260</b>	<b>8.26±0.15</b>	<b>0.76±0.07</b>	<b>0.80±0.14</b>	<b>3.26±0.53</b>	<b>0.37<sup>+0.08</sup><sub>-0.07</sub></b>	<b>1.17<sup>+0.16</sup><sub>-0.16</sub></b>	<b>68</b>	<b>2.97</b>
LP888-64	9530±310	7.92±0.12	0.56±0.05	0.58±0.07	1.34±0.52	4.5 <sup>+3.3</sup> <sub>-2.1</sub>	5.1 <sup>+3.3</sup> <sub>-2.1</sub>	11	4.23
WOLF672A	13330±570	7.85±0.10	0.53±0.04	0.22±0.03	1.00±0.44	10 <sup>+4</sup> <sub>-5</sub>	11 <sup>+4</sup> <sub>-5</sub>	2	4.19
NLTT10976	7050±200	7.68±0.25	0.40±0.15	0.99±0.12	-	-	-	-	3.52
NLTT29967	6180±220	7.26±0.45	0.14±0.19	0.55±0.23	-	-	-	-	1.89
NLTT44348	6510±190	7.42±0.33	0.23±0.14	0.63±0.20	-	-	-	-	2.34
<b>NLTT4615</b>	<b>5950±190</b>	<b>8.01±0.20</b>	<b>0.59±0.09</b>	<b>2.40±0.68</b>	<b>1.73±0.94</b>	<b>1.9<sup>+2.2</sup><sub>-0.9</sub></b>	<b>4.3<sup>+2.3</sup><sub>-1.1</sub></b>	<b>56</b>	<b>3.13</b>
<b>NLTT7890</b>	<b>5600±160</b>	<b>8.01±0.20</b>	<b>0.59±0.09</b>	<b>2.99±0.78</b>	<b>1.71±0.94</b>	<b>2.0<sup>+2.3</sup><sub>-0.9</sub></b>	<b>5.0<sup>+2.5</sup><sub>-1.2</sub></b>	<b>60</b>	<b>1.90</b>
<b>G107-70</b>	<b>5210± 60</b>	<b>8.01±0.20</b>	<b>0.59±0.09</b>	<b>3.90±1.00</b>	<b>1.69±0.94</b>	<b>2.0<sup>+2.5</sup><sub>-1.0</sub></b>	<b>5.9<sup>+2.7</sup><sub>-1.4</sub></b>	<b>66</b>	<b>4.38</b>
<b>NLTT1374</b>	<b>9290±330</b>	<b>8.01±0.20</b>	<b>0.60±0.09</b>	<b>0.70±0.12</b>	<b>1.83±0.92</b>	<b>1.6<sup>+1.6</sup><sub>-0.6</sub></b>	<b>2.3<sup>+1.6</sup><sub>-0.7</sub></b>	<b>31</b>	<b>2.19</b>
<b>NLTT7051</b>	<b>7630±220</b>	<b>8.01±0.20</b>	<b>0.60±0.09</b>	<b>1.16±0.22</b>	<b>1.78±0.93</b>	<b>1.7<sup>+1.8</sup><sub>-0.7</sub></b>	<b>2.8<sup>+1.8</sup><sub>-0.8</sub></b>	<b>41</b>	<b>2.97</b>
<b>NLT13599</b>	<b>5400± 80</b>	<b>8.01±0.20</b>	<b>0.59±0.09</b>	<b>3.41±0.87</b>	<b>1.70±0.95</b>	<b>2.0<sup>+2.4</sup><sub>-0.9</sub></b>	<b>5.4<sup>+2.6</sup><sub>-1.3</sub></b>	<b>63</b>	<b>2.47</b>
<b>NLTT15796</b>	<b>5025±60</b>	<b>8.01±0.20</b>	<b>0.59±0.09</b>	<b>4.60±0.88</b>	<b>1.68±0.95</b>	<b>2.1<sup>+2.6</sup><sub>-1.0</sub></b>	<b>6.7<sup>+2.8</sup><sub>-1.3</sub></b>	<b>69</b>	<b>4.31</b>
<b>NLT55288</b>	<b>6510±170</b>	<b>8.01±0.20</b>	<b>0.60±0.09</b>	<b>1.77±0.43</b>	<b>1.75±0.94</b>	<b>1.8<sup>+2.1</sup><sub>-0.8</sub></b>	<b>3.6<sup>+2.1</sup><sub>-0.9</sub></b>	<b>49</b>	<b>1.21</b>
<b>L577-71</b>	<b>8150±110</b>	<b>8.01±0.20</b>	<b>0.60±0.09</b>	<b>0.98±0.17</b>	<b>1.79±0.92</b>	<b>1.6<sup>+1.7</sup><sub>-0.7</sub></b>	<b>2.6<sup>+1.7</sup><sub>-0.7</sub></b>	<b>37</b>	<b>4.08</b>

**Notes.** The WDs with  $t_{\text{cool}}/\text{Age}$  ratio greater than 30% are highlighted in boldface.

wide binary system. The results for the sample are collected in Table 8. For NLTT19314 and WOLF672B, we could not directly perform a photometric distance determination since their estimated ages are greater than 8 Gyr, which is the age limit of the models we used. Thus, we just adopted a value of 8 Gyr, since the evolutionary changes of these stars between 8 and 13 Gyr are negligible.

## 7. Discussion

The main product of this part of the work is the determination of ages for 27 low-mass stars that are members of wide binary pairs. For eighteen of these age determinations we employed WD atmospheric parameters coming from a detailed spectroscopic fit, while for nine additional systems we used photometric  $T_{\text{eff}}$  values and an estimated  $\log g$  from the average of the rest. The final age is the sum of two contributions, namely the cooling time of the WD and the lifetime of the progenitor, mostly during the main sequence. As can be seen in Table 7, there is a clear distinction between the subsamples with spectroscopic and pho-

tometric temperatures in that the former shows relatively short cooling ages (usually  $< 1$  Gyr), while these are significantly longer for the latter ( $\sim 1-5$  Gyr). This is not a coincidence since older WDs are cooler and the Balmer lines in their spectrum are weak or nonexistent.

To further exploit our sample, it is worth evaluating the reliability of our estimated ages. The uncertainties we provide in Table 7 come from the random error estimates related to our fitting procedure, but they do not include systematic contributions potentially arising from the relationships and models used. We are not especially concerned with the contribution from models since the WD cooling process is relatively simple and main-sequence lifetime estimates should be quite reliable. However, there is some degree of concern as to the possible existence of systematic uncertainties related to the initial-final mass relationship of WDs. Many improvements have been achieved during these last years, for instance with the coverage of the low-mass domain (Catalán et al. 2008a). However, there is still a relatively large cosmic dispersion in the empirical initial-final mass relationship that could be related, e.g., to metallicity effects or the

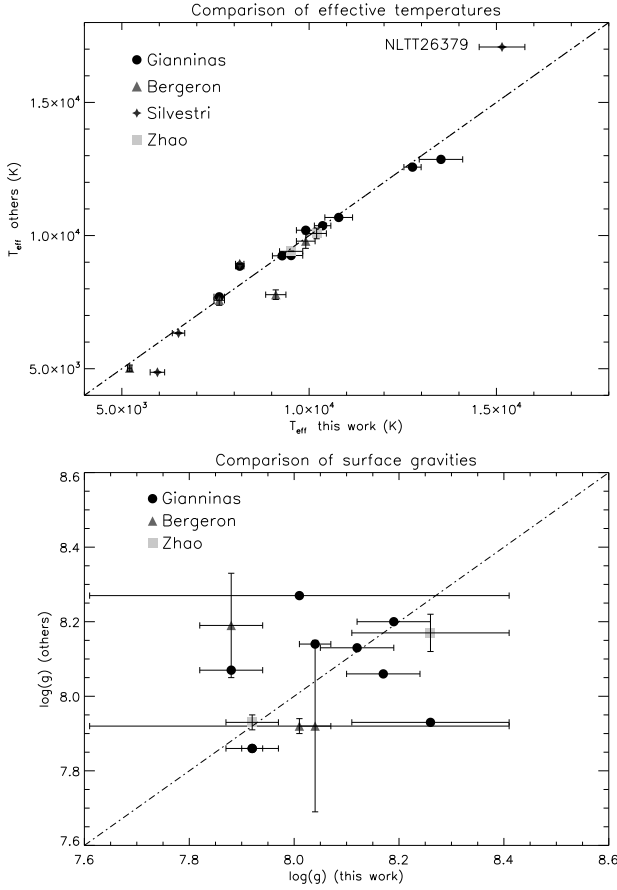


**Fig. 6.** Comparison of  $T_{\text{eff}}$  (top) and  $\log g$  (bottom) determined by us with values obtained by Bergeron et al. (2001), Silvestri et al. (2001), Gianninas et al. (2005), and Zhao et al. (2011). The dashed line is the 1:1 correspondence.

**Table 8.** Distances of the low-mass members of the wide binary sample.

Star	$d$ (pc)	Star	$d$ (pc)
NLTT1759	$105 \pm 15^*$	NLTT58108	$90 \pm 10$
NLTT10977	$60 \pm 5$	G86-B1A	$25 \pm 5$
NLTT13109	$20 \pm 5^*$	LP347-5	$8 \pm 5$
NLTT15797	$40 \pm 5^*$	LP856-54	$45 \pm 5$
NLTT19314	$45 \pm 20$	LP888-63	$15 \pm 5$
NLTT21892	$30 \pm 5^*$	WOLF672B	$15 \pm 5$
NLTT26385	$15 \pm 5$	NLTT4616	$35 \pm 5$
NLTT28469	$15 \pm 5$	NLTT7887	$45 \pm 5$
NLTT28711	$55 \pm 15^*$	G107-69	$10 \pm 5$
NLTT28771	$50 \pm 5$	NLTT1370	$125 \pm 10$
NLTT29948	$45 \pm 5^*$	NLTT7055	$65 \pm 5$
NLTT31647	$25 \pm 5$	NLTT13601	$30 \pm 5^*$
NLTT31888	$80 \pm 5$	NLTT55287	$35 \pm 5^*$
NLTT39608	$60 \pm 5$	L577-72	$15 \pm 5$
NLTT44344	$55 \pm 5$		
NLTT56548	$60 \pm 5$		

**Notes.** \* nine low-mass stars with trigonometric parallax information.

poorly-known mass-loss processes during the AGB phase. For this reason, we believe that  $t_{\text{cool}}$  is more reliable than  $t_{\text{prog}}$ .

Given the considerations above, we favour systems in which the contribution of WD cooling time to the total age is at its maximum. In addition, we aim at defining a sample of companion

**Table 9.**  $V-J$  colour and age for stars with  $t_{\text{cool}}$  vs. total age ratio  $> 30\%$ , separated in spectral type bins and sorted by age within each bin.

$V-J$	Age	$V-J$	Age
<i>Early K</i>		<i>Early-mid M</i>	
1.46	$1.17^{+0.14}_{-0.13}$	3.85	$1.58^{+0.18}_{-0.20}$
1.21	$3.6^{+2.1}_{-0.9}$	3.67	$1.64^{+0.20}_{-0.20}$
1.90	$5.0^{+2.5}_{-1.2}$	3.21	$3.9^{+2.6}_{-1.1}$
<i>Late K</i>		<i>Mid-late M</i>	
2.19	$2.3^{+1.6}_{-0.7}$	4.18	$1.58^{+0.27}_{-0.20}$
2.47	$5.4^{+2.6}_{-1.3}$	4.19	$1.77^{+0.71}_{-0.35}$
<i>Early M</i>		4.08	$2.6^{+0.7}_{-1.7}$
2.95	$1.13^{+0.08}_{-0.07}$	4.38	$5.9^{+2.7}_{-1.4}$
2.97	$1.17^{+0.15}_{-0.14}$	4.31	$6.7^{+2.8}_{-1.3}$
2.97	$2.8^{+1.8}_{-0.8}$		
3.13	$4.3^{+0.8}_{-1.1}$		

stars with a wide range of spectral types that cover as much of the important 1-6 Gyr age interval as possible. From these two premises, we found that a constraint of  $t_{\text{cool}}/\text{Age} > 30\%$  gives the best compromise between age robustness and sample size, so therefore selected systems fulfilling this requirement. These objects are highlighted in boldface in Table 7. Eighteen systems in our sample fulfil this condition. Almost all of the cooler WDs analysed in this work belong to this reliable sample, which is expected because their cooling times are relatively long. The last column of Table 7 includes, for reference, the  $V - J$  index of the companion to each WD so that the proper sample selection for the next step can be made. Following the same prescription as was used in the *Sun in Time* project, one should define the spectral type (or mass, or  $V - J$ ) intervals and select stars that cover a wide age range. Given the  $V - J$  colours of our sample stars, we grouped them into five bins, namely early K, late K, early M, early-mid M, and mid-late M. Table 9 shows these bins with the  $V - J$  and ages of the stars included in them. Each bin has at least two stars (to be added to the cluster averages presented in §2), covering roughly the interval between 1 and 5 Gyr. These are the stars for which we collect activity information so that they can be used to trace the time-evolution of their high-energy emissions from the start of the zero-age main-sequence to at least the age of our Sun. This is illustrated in Fig. 7, which is the same as Fig. 1 but with vertical lines showing the position of the ages that will be sampled with the stars we have analysed. The new ages cover the relevant area that is currently unpopulated and beyond what can be studied with open cluster data.

## 8. Conclusions

We studied a sample of 30 wide binary systems composed of a WD component and a low-mass companion. We have obtained high-signal-to-noise low resolution spectroscopy for 25 of the WDs, which allowed us to carry out a full analysis of their spectra and a fit of WD models to derive atmospheric parameters,  $T_{\text{eff}}$  and  $\log g$ . Total ages for the wide binary systems were obtained from a procedure based on the cooling sequences of Salaris et al. (2000), the initial-final mass relationship of Catalán et al. (2008a), and the stellar tracks of Domínguez et al. (1999). We estimate that the total ages for 18 of the systems are especially reliable as the relative contribution from the cooling time of the WD (which is supposed to be relatively unaffected by systematic errors) is greater than 30%. The resulting sample covers spectral types from early K to mid-late M and, very importantly, it contains stars that populate the critical age interval

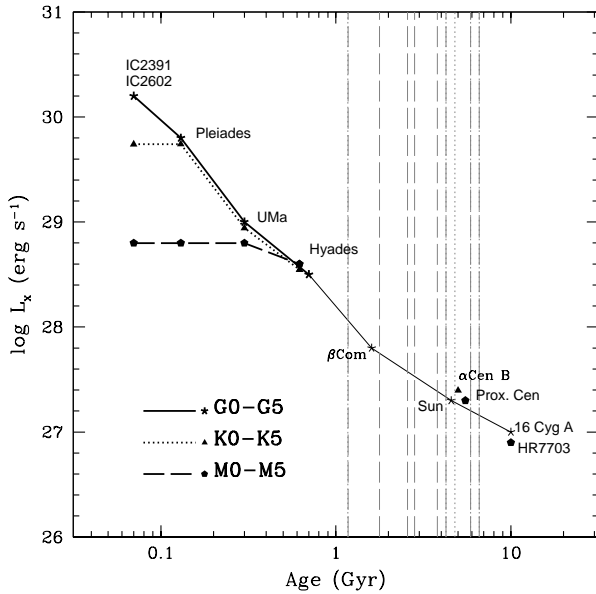


**Fig. 7.**  $\log L_X$  vs. age diagram for G0-G5, K0-K5, and M0-M5 spectral type bins. The vertical lines correspond to the ages of the WDs with reliable age determinations from our study. The G0-G5 spectral type interval is already fully covered from the *The Sun in Time* project.

between 1 and 5 Gyr for which the determination of ages using other methods is difficult. Most of our targets are within a few tens of parsecs, so the study of their activity properties is much easier than for stars belonging to intermediate- or old-age clusters.

For the selected stars we are obtaining high-resolution spectroscopy to measure chromospheric fluxes and X-ray data so that we can build reliable relationships describing the time evolution of emissions related to stellar magnetic activity. As our final goal, our work should provide critical input information to any effort of understanding the long-term evolution of the atmospheres of planets around low-mass stars, including their potential habitability. It will also allow better understanding of the evolution of high-energy emissions from low-mass stars. The activity-age relationship will allow us not only to address the time evolution of high energy radiation, but also to use it as an age calibrator when the stellar high-energy emissions can be measured. This age indicator is very interesting because it will be based on the star's own properties and will be useful in a regime ( $> 1$  Gyr) where estimating stellar ages is still very difficult.

*Acknowledgements.* We thank D. Koester for providing us with his white dwarf models. We acknowledge support from the Spanish MICINN grant AYA2009-06934. S.C. is supported by a Marie Curie Intra-European Fellowship within the 7th European Community Framework Programme.

## References

Ayres, T. R. 1997, *J. Geophys. Res.*, 102, 1641  
 Baraffe, I., Chabrier, G., Allard, F., & Hauschildt, P. H. 1997, *A&A*, 327, 1054  
 Bergeron, P., Leggett, S. K., & Ruiz, M. T. 2001, *ApJS*, 133, 413  
 Bergeron, P., Wesemael, F., & Fontaine, G. 1992, *ApJ*, 387, 288  
 Catalán, S., Isern, J., García-Berro, E., & Ribas, I. 2008a, *MNRAS*, 387, 1693  
 Catalán, S., Isern, J., García-Berro, E., et al. 2008b, *A&A*, 477, 213  
 Chanamé, J. & Gould, A. 2004, *ApJ*, 601, 289  
 Domínguez, I., Chieffi, A., Limongi, M., & Straniero, O. 1999, *ApJ*, 524, 226  
 Fontaine, G., Brassard, P., & Bergeron, P. 2001, *PASP*, 113, 409  
 Gianninas, A., Bergeron, P., & Fontaine, G. 2005, *ApJ*, 631, 1100

Gould, A. & Chanamé, J. 2004, *ApJS*, 150, 455  
 Holberg, J. B. & Bergeron, P. 2006, *AJ*, 132, 1221  
 Jeffries, R. D., Jackson, R. J., Briggs, K. R., Evans, P. A., & Pye, J. P. 2010, *MNRAS*, 1858  
 Johnson, H. L., Iriarte, B., Mitchell, R. I., & Wisniewski, W. Z. 1966, *Communications of the lunar and planetary laboratory*, 4, 99  
 Lammer, H., Selsis, F., Ribas, I., et al. 2003, in *ESA Special Publication*, Vol. 539, *Earths: DARWIN/TPF and the Search for Extrasolar Terrestrial Planets*, ed. M. Fridlund, T. Henning, & H. Lacoste, 491–496  
 Luyten, W. J. 1979-1980, *New Luyten Catalogue of Stars with Proper Motions Larger than Two Tenths of an Arcsecond*, (Minneapolis: Univ. Minnesota Press)  
 Mamajek, E. E. & Hillenbrand, L. A. 2008, *ApJ*, 687, 1264  
 Masana, E., Jordi, C., & Ribas, I. 2006, *A&A*, 450, 735  
 McCook, G. P. & Sion, E. M. 1999, *ApJS*, 121, 1  
 McCook, G. P. & Sion, E. M. 2006, *VizieR Online Data Catalog*, 3235, 0  
 Montes, D., López-Santiago, J., Gálvez, M. C., et al. 2001, *MNRAS*, 328, 45  
 Oswalt, T. D., Hintzen, P., & Luyten, W. 1988, *ApJS*, 66, 391  
 Penz, T., Micela, G., & Lammer, H. 2008, *A&A*, 477, 309  
 Pizzolato, N., Maggio, A., Micela, G., Sciortino, S., & Ventura, P. 2003, *A&A*, 397, 147  
 Porto de Mello, G. F., Lyra, W., & Keller, G. R. 2008, *A&A*, 488, 653  
 Press, W. H., Teukolsky, S. A., Vetterling, W. T., & Flannery, B. P. 1992, *Numerical recipes in FORTRAN. The art of scientific computing* (Cambridge: University Press, —c1992, 2nd ed.)  
 Ribas, I., Guinan, E. F., Güdel, M., & Audard, M. 2005, *ApJ*, 622, 680  
 Salaris, M. 2009, in *IAU Symposium*, Vol. 258, *IAU Symposium*, ed. E. E. Mamajek, D. R. Soderblom, & R. F. G. Wyse, 287–298  
 Salaris, M., García-Berro, E., Hernanz, M., Isern, J., & Saumon, D. 2000, *ApJ*, 544, 1036  
 Schmitt, J. H. M. M., Fleming, T. A., & Giampapa, M. S. 1995, *ApJ*, 450, 392  
 Silvestri, N. M., Hawley, S. L., & Oswalt, T. D. 2005, *AJ*, 129, 2428  
 Silvestri, N. M., Oswalt, T. D., Wood, M. A., et al. 2001, *AJ*, 121, 503  
 Skumanich, A. 1972, *ApJ*, 171, 565  
 Soderblom, D. R. 2010, *ARA&A*, 48, 581  
 Stepień, K., Schmitt, J. H. M. M., & Voges, W. 2001, *A&A*, 370, 157  
 Tremblay, P. & Bergeron, P. 2009, *ApJ*, 696, 1755  
 Zhao, J. K., Oswalt, T. D., Rudkin, M., Zhao, G., & Chen, Y. Q. 2011, *ArXiv*: 1101.3257